

A Model of Fluid-Structure and Biochemical Interactions with Applications to Subclinical Leaflet Thrombosis

Aaron Barrett^{1,*}, Jordan A. Brown², Margaret Anne Smith², Andrew Woodward³, John P. Vavalle^{4,5}, Arash Kheradvar⁶, Boyce E. Griffith^{7,8,9,10}, and Aaron L. Fogelson¹¹

¹Department of Mathematics, University of Utah, Salt Lake City, UT, USA

²Department of Mathematics, University of North Carolina, Chapel Hill, NC, USA

³Advanced Medical Imaging Lab, University of North Carolina Medical Center, Chapel Hill, NC, USA

⁴University of North Carolina School of Medicine, Chapel Hill, NC, USA

⁵Division of Cardiology, Department of Medicine, University of North Carolina, Chapel Hill, NC, USA

⁶Department of Biomedical Engineering, University of California Irvine, Irvine, CA, USA

⁷Departments of Mathematics, Applied Physical Sciences, and Biomedical Engineering, University of North Carolina, Chapel Hill, NC, USA

⁸Carolina Center for Interdisciplinary Applied Mathematics, University of North Carolina, Chapel Hill, NC, USA

⁹Computational Medicine Program, University of North Carolina, Chapel Hill, NC, USA

¹⁰McAllister Heart Institute, University of North Carolina, Chapel Hill, NC, USA

¹¹Departments of Mathematics and Biomedical Engineering, University of Utah, Salt Lake City, UT, USA

*barrett@math.utah.edu

Abstract

Subclinical leaflet thrombosis (SLT) is a potentially serious complication of aortic valve replacement with a bioprosthetic valve in which blood clots form on the replacement valve. SLT is associated with increased risk of transient ischemic attacks and strokes and can progress to clinical leaflet thrombosis. SLT following aortic valve replacement also may be related to subsequent structural valve deterioration, which can impair the durability of the valve replacement. Because of the difficulty in clinical imaging of SLT, models are needed to determine the mechanisms of SLT and could eventually predict which patients will develop SLT. To this end, we develop methods to simulate leaflet thrombosis that combine fluid-structure interaction and a simplified thrombosis model that allows for deposition along the moving leaflets. Additionally, this model can be adapted to model deposition or absorption along other moving boundaries. We present both convergence results and quantify the model's ability to realize changes in stroke volume and pressures. These new approaches are an important advancement in thrombosis modeling in that it incorporates both adhesion to the surface of the leaflets and feedback to the fluid-structure interaction.

1 Introduction

Subclinical leaflet thrombosis is a potentially serious complication of bioprosthetic aortic valve replacement and may occur following either surgical or transcatheter aortic valve replacement.

Although bioprosthetic heart valves (BHVs) are remarkably less thrombogenic than mechanical heart valves (MHVs), clinical valve thrombosis can occur as a life-threatening complication. Recent studies [25, 26, 36] have suggested that the rate of subclinical leaflet thrombosis (SLT) is as high as 13–38% [34]. SLT is associated with increased risk of transient ischemic attacks and strokes, acute myocardial infarction, and accelerated valve deterioration [32]. Further, if left untreated, SLT can progress to clinical valve thrombosis. While a cardiac computed tomography (CT) scan can detect SLT, predicting which patients will develop SLT is currently not possible. Accordingly, there is a need for computational tools to model the fluid-structure and biochemical interactions that predispose a particular patient to develop SLT.

Prior work to model leaflet thrombosis has focused on direct computational fluid dynamics (CFD) simulations of blood flow through the valve. Plitman Mayo et al. [31] performed CFD experiments of deployed transcatheter aortic valve replacements (TAVRs) to determine areas of stagnated blood flow, suggesting possible sites of thrombosis formation. Vahidkhah et al. [42] compared blood residence times in the coronary and non-coronary leaflets after a TAVR procedure and determined similar residence times for all the leaflets. Kivi et al. [20] performed two dimensional fluid-structure interaction (FSI) simulations with leaflets of varying stiffness. A common finding in CFD simulations is the presence of stagnant regions in the aortic sinus, in which blood clots are thought to form. Hatoum et al. [17] combined a CFD model of flow through patient specific geometry post-TAVR with a reduced order model that predicted thrombus growth based on the wall shear stress and percent stasis volume measurements. While they were able to determine a correlation between circulation and amount of thrombosis, they concluded that finer flow metrics or FSI analysis are needed to fully predict thrombosis.

Mathematical and computational models of thrombosis have also been developed, but methods suitable for modeling thrombosis on dynamic flexible structures, which is critical for describing leaflet thrombosis, are lacking. Fogelson et al. [10] developed a model of intravascular platelet deposition and determined the sensitivity of thrombus formation due to various chemical and platelet factors. Du and Fogelson [7] developed a multiphase model of platelet aggregation in which the thrombus is modeled as a viscoelastic fluid. This model can be seen as an extension of models by Fogelson and Guy [9] that were created to study thrombus formation in a moving fluid. Models describing flowing platelets and platelet deposition onto a stationary vessel wall have been developed using a variety of multiscale modeling and computational approaches [6, 40, 43, 46]. These models describe both fluid-phase transport of platelets and the influence of platelet deposits on the hemodynamics through and near the deposits. In these models, the platelets deposit over stationary surfaces. However, to our knowledge, no thrombosis model has yet been developed that allows for thrombus growth on a surface whose motion is determined by solving an FSI problem, e.g., a heart valve leaflet.

The present study introduces new numerical methods and a simplified mathematical model of leaflet thrombosis that incorporates a mass deposition model together with fluid-structure interaction. The mass deposition model includes a fluid-phase field that can be interpreted as free-moving platelets and a structure-bound field that can be interpreted as bound platelets. The deposition

model is incorporated into an FSI model of the aortic valve on which platelets would deposit and alter the leaflet stiffness according to the concentration of bound platelets.

2 Continuous Equations

We consider an FSI model of thrombus formation on the aortic valve leaflets. The valve geometry is created via slicing a three-dimensional reconstruction of a typical trileaflet aortic valve, as will be discussed further in section 3.1. In this simplified model, fluid phase platelets can bind to the leaflet surface while the surface-bound platelets stiffen the leaflets and can also dissociate back into the fluid.

2.1 Fluid-Structure Interaction

The fluid-structure system is modeled using the immersed finite element/finite difference method [16]. In this approach, a fixed computational domain Ω is partitioned into a time-dependent fluid subdomain Ω_t^f and a time-dependent solid subdomain Ω_t^s , so that $\Omega = \Omega_t^f \cup \Omega_t^s$. The fluid domain is further subdivided into the lumen Ω_t^{f-} (i.e., the space occupied by the blood, in which platelets are free to advect and diffuse) and the space outside the aortic root Ω_t^{f+} , with $\Omega_t^f = \Omega_t^{f-} \cap \Omega_t^{f+}$; see figure 1. We denote Eulerian physical coordinates with \mathbf{x} . The solid domain is tracked using Lagrangian material coordinates \mathbf{X} , and the mapping between the reference and current coordinates is $\chi(\mathbf{X}, t)$. The motion of the fluid-structure system is described by

$$\rho \frac{D\mathbf{u}}{Dt}(\mathbf{x}, t) = -\nabla p(\mathbf{x}, t) + \mu \nabla^2 \mathbf{u}(\mathbf{x}, t) + \mathbf{f}(\mathbf{x}, t), \quad (1a)$$

$$\nabla \cdot \mathbf{u}(\mathbf{x}, t) = 0, \quad (1b)$$

$$\mathbf{f}(\mathbf{x}, t) = \int_{\Omega_0^s} \mathbf{F}(\mathbf{X}, t) \delta(\mathbf{x} - \chi(\mathbf{X}, t)) d\mathbf{X}, \quad (1c)$$

$$\frac{\partial \chi}{\partial t}(\mathbf{X}, t) = \int_{\Omega} \mathbf{u}(\mathbf{x}, t) \delta(\mathbf{x} - \chi(\mathbf{X}, t)) d\mathbf{x} = \mathbf{u}(\chi(\mathbf{X}, t), t), \quad (1d)$$

in which $\frac{D}{Dt}$ is the material derivative, $\mathbf{u}(\mathbf{x}, t)$ and $p(\mathbf{x}, t)$ are the Eulerian velocity and pressure, respectively, $\mathbf{f}(\mathbf{x}, t)$ is the Eulerian force density, $\mathbf{F}(\mathbf{X}, t)$ is the Lagrangian force density, which is determined in a manner specified below, and $\delta(\mathbf{x})$ is the Dirac delta function. The fluid density ρ and viscosity μ are assumed to be constant. Equations (1a) and (1b) are the well known Navier-Stokes equations and hold across the entire computational domain Ω . Equations (1c) and (1d) couple the Lagrangian and Eulerian variables.

Our model considers both rigid and elastic structures. For rigid structures, we use a penalty formulation that tethers the structure in place via

$$\mathbf{F}(\mathbf{X}, t) = \kappa(\mathbf{X} - \chi(\mathbf{X}, t)), \quad (2)$$

in which κ is the stiffness parameter [23]. In practice, we choose κ to be the largest stable value permitted by the numerical scheme so that the structure's motion is minimized.

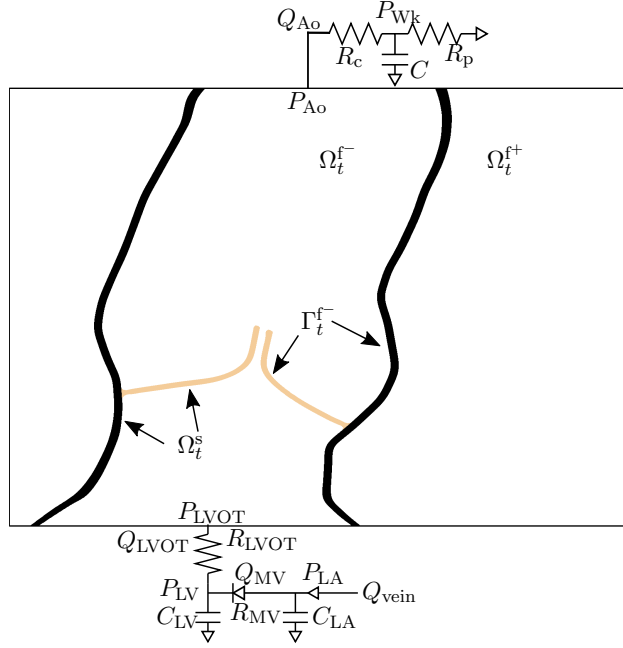


Figure 1: The domain is decomposed into a solid subdomain Ω_t^s and a fluid subdomain Ω_t^f , which itself is partitioned into interior subregion Ω_t^{f-} , which corresponds to the lumen, and an exterior subregion Ω_t^{f+} , which corresponds to the space outside the vessel. The left ventricular outflow tract (LVOT) boundary conditions are determined via a time-dependent elastance-based model of the left heart, including the left ventricle (LV), mitral valve (MV) and left atrium (LA). The boundary conditions at the outlet of the ascending aorta are determined via a three element Windkessel model.

For elastic structures, the response is given by the first Piola-Kirchhoff stress \mathbb{P} , which is determined from a strain-energy function $\Psi(\mathbb{F})$ via $\mathbb{P} = \frac{\partial \Psi}{\partial \mathbb{F}}$, in which $\mathbb{F} = \frac{\partial \mathbf{X}}{\partial \mathbf{X}_0}$ is the deformation gradient tensor. Following the immersed finite element/difference approach of Vadala-Roth et al. [41], we split the strain energy functional into deviatoric and dilational parts, $\Psi(\mathbb{F}) = W(\bar{\mathbb{F}}) + U(J)$, in which $J = \det \mathbb{F}$ is the Jacobian of the deformation tensor and $\bar{\mathbb{F}} = J^{-1/3} \mathbb{F}$. In what follows, we choose the dilational part of the energy to be

$$U(J) = \frac{\kappa_{\text{stab}}}{2} (\log J)^2. \quad (3)$$

The Lagrangian force density is then computed by requiring

$$\int_{\Omega_0^s} \mathbf{F}(\mathbf{X}, t) \cdot \mathbf{V}(\mathbf{X}) d\mathbf{X} = - \int_{\Omega_0^s} \mathbb{P}(\mathbf{X}, t) : \nabla_{\mathbf{X}} \mathbf{V}(\mathbf{X}) d\mathbf{X}, \quad (4)$$

for all smooth test functions $\mathbf{V}(\mathbf{X})$.

The aortic wall is modeled as a rigid structure. The leaflets are modeled as a hyperelastic material that follows an exponential neo-Hookean model [13, 28]. The deviatoric strain energy functional for this model is given by

$$W(\bar{\mathbb{F}}) = C_{10} \left(e^{C_{01}(\bar{I}_1 - 3)} - 1 \right), \quad (5)$$

in which C_{10} and C_{01} are material constants and \bar{I}_1 is the first deviatoric strain invariant of the modified right Cauchy-Green tensor, $\bar{I}_1 = \text{tr}(\bar{\mathbb{C}})$, which is defined in terms of the modified deformation tensor, $\bar{\mathbb{C}} = \bar{\mathbb{F}}^T \bar{\mathbb{F}}$.

2.2 Boundary Conditions

We use reduced order models to determine pressure-flow relationships in the ascending aorta and left ventricular outflow tract (LVOT); see figure 1. These reduced order models are connected to the FSI model through boundary conditions imposed on the fluid [15, 22]. We use a coupling scheme in which the net flow rate through the boundary surface serves as an input to the reduced order models. In turn, the reduced order models determine a corresponding pressure that is prescribed on the boundary surface. On the remainder of the computational domain's boundary, we use zero velocity boundary conditions.

We use a three-element Windkessel model [38] for the downstream reduced order model,

$$C \frac{dP_{\text{Wk}}}{dt} = Q_{\text{Ao}} - \frac{P_{\text{Wk}}}{R_{\text{p}}}, \quad (6)$$

$$P_{\text{Ao}} = P_{\text{Wk}} + Q_{\text{Ao}} R_{\text{c}}, \quad (7)$$

in which C is the compliance, R_{c} is the characteristic resistance, R_{p} is the peripheral resistance, P_{Wk} is the Windkessel pressure, and Q_{Ao} and P_{Ao} are the volumetric flow rate and pressure at the outlet of the ascending aorta.

For the upstream model, we employ a time-dependent elastance-based left heart model [38],

$$\frac{d(C_{\text{LA}}P_{\text{LA}})}{dt} = Q_{\text{vein}} - Q_{\text{MV}}, \quad (8)$$

$$\frac{d(C_{\text{LV}}P_{\text{LV}})}{dt} = Q_{\text{MV}} - Q_{\text{LVOT}}, \quad (9)$$

$$P_{\text{LVOT}} = P_{\text{LV}} - Q_{\text{LVOT}}R_{\text{LVOT}}, \quad (10)$$

$$Q_{\text{MV}} = \begin{cases} 0, & \text{if } P_{\text{LA}} \leq P_{\text{LV}}, \\ \frac{P_{\text{LA}} - P_{\text{LV}}}{R_{\text{MV}}}, & \text{if } P_{\text{LA}} > P_{\text{LV}}, \end{cases} \quad (11)$$

in which C_{LA} and C_{LV} are the time-dependent compliances of the left atrium and left ventricle, respectively. The R_{LVOT} and R_{MV} are the resistances of the LVOT and mitral valve, the latter of which is modeled as a diode. The P_{LA} and P_{LV} are the left atrial and ventricular pressures, and Q_{vein} , Q_{MV} , and Q_{LVOT} are the volumetric flow rates of the pulmonary veins, mitral valve, and LVOT. In this model, Q_{vein} is prescribed as a constant inflow rate into the left atrium. We set the compliances C_{LA} and C_{LV} using the “two-Hill” function waveform for the elastance $E(t) = \frac{1}{C(t)}$ [30],

$$E(t) = k \left(\frac{g_1}{1 + g_1} \right) \left(\frac{1}{1 + g_2} \right) + E_{\min}, \quad (12)$$

$$g_i = \left(\frac{t}{\tau_i} \right)^{m_i}, \quad (13)$$

$$k = \frac{E_{\max} - E_{\min}}{\max \left(\frac{g_1}{1 + g_1}, \frac{1}{1 + g_2} \right)}. \quad (14)$$

We use the elastance parameters for the left atrium from Mynard et al. [30]. The remaining parameters are fit to experimental measurements of human aortic pressures P_{Ao} and aortic flow rates Q_{Ao} from Murgo et al. [29] by taking the experimental measurements of Q_{Ao} as input to the Windkessel model, and comparing the resulting values of P_{Ao} to its experimental values. We calculate the best-fit parameters to data from Murgo et al. [30] for a “Type A” beat for the upstream model and its corresponding downstream counterpart independently, using MATLAB’s `fmincon`, a nonlinear optimization tool.

2.3 Mass Deposition Model

We couple the FSI model to a mass deposition model that includes a fluid-phase $c_f(\mathbf{x}, t)$ concentration measured per unit current volume and a surface-bound $C_b(\mathbf{X}, t)$ concentration field measured per unit reference area. Although this model does not include the cellular and biochemical interactions describing thrombosis, it does include fields which we view as platelet populations, and the conversion of fluid-phase platelets in c_f to surface-bound platelets in C_b as platelet adhesion. The fluid-phase species diffuses and advects with the local fluid velocity in the interior fluid domain Ω_t^f and can convert into the surface-bound species along the boundary $\Gamma_t \subset \Gamma_t^f = \partial\Omega_t^f$. The surface-bound species moves with the structure and can dissociate into the fluid-phase species. The

model equations are

$$\frac{\partial c_f(\mathbf{x}, t)}{\partial t} + \mathbf{u}(\mathbf{x}, t) \cdot \nabla c_f(\mathbf{x}, t) = D \nabla^2 c_f(\mathbf{x}, t), \quad \mathbf{x} \in \Omega_t^f, \quad (15a)$$

$$\begin{aligned} -D \frac{\partial c_f(\mathbf{x}, t)}{\partial \mathbf{n}} &= k_{\text{on}}(C_b^{\text{max}} - C_b(\chi(\mathbf{X}, t), t)) J_s c_f(\mathbf{x}, t) \\ &\quad - k_{\text{off}} C_b(\chi(\mathbf{X}, t), t) J_s, \quad \mathbf{x} \in \Gamma_t, \end{aligned} \quad (15b)$$

$$\begin{aligned} \frac{\partial C_b(\mathbf{X}, t)}{\partial t} &= k_{\text{on}}(C_b^{\text{max}} - C_b(\mathbf{X}, t)) c_f(\chi(\mathbf{X}, t), t) \\ &\quad - k_{\text{off}} C_b(\mathbf{X}, t), \quad \mathbf{X} \in \Gamma_0, \end{aligned} \quad (15c)$$

$$\frac{\partial c_f(\mathbf{x}, t)}{\partial \mathbf{n}} = 0, \quad \mathbf{x} \in \Gamma_t^f \setminus \Gamma_t, \quad (15d)$$

in which D is the diffusion coefficient, k_{on} and k_{off} are the reaction rates for adhesion and dissociation, respectively, C_b^{max} is the carrying capacity of C_b per unit undeformed area along the boundary Γ_0 , and $J_s = \frac{dA}{da}$ is the surface Jacobian, which is the ratio of reference and current areas.

To model the effect of thrombosis over the valve leaflets, we set the stiffness coefficient of the leaflets C_{10} to be a function of the surface concentration $C_b(\mathbf{X}, t)$. Because $C_b(\mathbf{X}, t)$ is defined only on the surface of the leaflet, we use a harmonic interpolation procedure to extend the surface concentration into the interior of the leaflet, where the Lagrangian forces are calculated. Specifically, we solve Laplace's equation

$$\nabla^2 C_b^{\text{in}}(\mathbf{X}, t) = 0, \quad \mathbf{X} \in \Omega_0^{\text{leaf}}, \quad (16)$$

$$C_b^{\text{in}}(\mathbf{X}, t) = \begin{cases} C_b(\mathbf{X}, t), & \text{if } \mathbf{X} \in \Gamma_0, \\ 0, & \text{otherwise,} \end{cases} \quad (17)$$

in which Ω_0^{leaf} is the leaflet domain in the initial configuration. Having found $C_b^{\text{in}}(\mathbf{X}, t)$, we then set the stiffness of the leaflet to be

$$C_{10}(C_b^{\text{in}}) = C_{10}^{\text{base}} \left(\frac{\beta + 1}{2} - \frac{\beta - 1}{2} \cos \left(\frac{\pi C_b^{\text{in}}}{C_b^{\text{max}}} \right) \right), \quad (18)$$

in which C_{10}^{base} is the stiffness with no accumulation and β is a multiplicative factor for the maximum stiffness.

The parameters of the mass deposition model are chosen so that the reactions occur on a similar time scale as the fluid-structure interactions. These values are several orders of magnitude larger than those used in a similar thrombosis model as described previously [9, 24]. The use of physically relevant parameters requires resolving multiple time scales and remains the topic of current research.

3 Computational Models and Numerical Methods

The model is implemented in IBAMR, which provides implementations of the immersed boundary method and several of its extensions along with support for adaptive mesh refinement [14]. IBAMR

utilizes libMesh for the finite element representation of the structural deformations [19] and PETSc for linear solvers [2, 3, 4]. Support for structured adaptive mesh refinement is provided by SAMRAI [18]. While the model can be naturally extended to three spatial dimensions, we describe the numerical implementation and results in two spatial dimensions.

3.1 Imaged Model and Mesh Generation

Our two-dimensional aortic root geometry is informed by a three-dimensional patient-specific aortic root model based on pre-procedural computed tomography (CT) image data of a female patient preparing for aortic valve replacement at UNC Medical Center. The images used in this study were obtained under a protocol approved by the UNC Institutional Review Board (study number 18-0202). The CT scan was performed using a Siemens SOMATOM Definition CT Scanner with an image resolution of $512 \times 512 \times 226$ and a voxel size of $0.441\,406\,25\text{ mm} \times 0.441\,406\,25\text{ mm} \times 0.6\text{ mm}$. The patient images are segmented by a semi-automated method in ITK-SNAP [44], which implements an active contour model that minimizes an energy functional of voxel intensities [45]. The aortic root measures 28 mm in diameter and 7.68 cm in length, and the thickness of the aortic wall is 1.0 mm. The inflow boundary of the model is truncated at the LVOT, and the outflow boundary of the model is truncated downstream of the aortic valve before the first arterial bifurcation. Artificial circular extensions are added at both boundaries using SOLIDWORKS (Dassault Systèmes SOLIDWORKS Corporation, Waltham, MA, USA) to simplify the application of boundary conditions to the computational model. The radius of the vessel at both truncations is 21 mm. Idealized aortic valve replacement leaflets with a thickness of 0.7 mm are created based on the measurements from Sahasakul et al. [35] and trimmed to fit within the reconstructed aortic root in SOLIDWORKS. To derive our two-dimensional aortic root geometry from the three-dimensional model, we extract a slice through the diameter of the aorta using Coreform Cubit (Computational Simulation Software, LLC, American Fork, UT, USA), which is a software application based on CUBIT from Sandia National Laboratory. We then use Cubit to smooth the angles in both the aortic root and leaflet surfaces and to generate structural meshes consisting of triangular elements.

3.2 Fluid-Structure Interaction

The fluid equations (1a) and (1b) are solved using a second-order staggered-grid finite difference method. The nonlinear term is approximated using a piecewise parabolic method [33]. The resulting saddle point system is solved using GMRES with a projection method as a preconditioner [15].

The immersed structure is discretized using \mathcal{C}^0 finite elements. A triangulation \mathcal{T}_h is constructed of the structure. The size of each element in the triangulation is chosen so that there is approximately one node per Cartesian grid cell. On \mathcal{T}_h , we define Lagrangian basis functions $\{\phi_l(\mathbf{X})\}_{l=1}^m$, in which m is the total number of nodes in the triangulation. We approximate the structural

deformation and force using the basis functions via

$$\chi(\mathbf{X}, t) = \sum_{l=1}^m \chi_l(t) \phi_l(\mathbf{X}), \quad (19)$$

$$\mathbf{F}(\mathbf{X}, t) = \sum_{l=1}^m \mathbf{F}_l(t) \phi_l(\mathbf{X}). \quad (20)$$

Coupling between the fluid and structure is mediated using regularized delta functions in equations (1c) and (1d). Recently, Lee and Griffith [23] suggested using delta functions with smaller support for structures in shear driven regimes. Therefore, in this work, we use the three-point B -spline kernel for the flexible valve leaflets, and a two-point piecewise linear kernel for the nearly rigid walls of the aortic root.

3.3 Mass Deposition Model

The fluid phase concentration field is approximated using a hybrid semi-Lagrangian cut-cell method [5]. For brevity, we omit the details of the discretization and only highlight the changes. To summarize, we split equation (15) into an advection step,

$$\frac{\partial c_f(\mathbf{x}, t)}{\partial t} + \mathbf{u}(\mathbf{x}, t) \cdot \nabla c_f(\mathbf{x}, t) = 0, \quad \mathbf{x} \in \Omega_t^{f-}, \quad (21)$$

and a diffusion step,

$$\begin{aligned} \frac{\partial c_f(\mathbf{x}, t)}{\partial t} &= D \nabla^2 c_f(\mathbf{x}, t), & \mathbf{x} \in \Omega_t^{f-}, & \\ -D \frac{\partial c_f(\mathbf{x}, t)}{\partial \mathbf{n}} &= k_{\text{on}}(C_b^{\text{max}} - C_b(\chi(\mathbf{X}, t), t)) J_s c_f(\mathbf{x}, t) & & \end{aligned} \quad (22a)$$

$$- k_{\text{off}} C_b(\chi(\mathbf{X}, t), t) J_s, \quad \mathbf{x} \in \Gamma_t, \quad (22b)$$

$$\begin{aligned} \frac{\partial C_b(\mathbf{X}, t)}{\partial t} &= k_{\text{on}}(C_b^{\text{max}} - C_b(\mathbf{X}, t)) c_f(\chi(\mathbf{X}, t), t) \\ &\quad - k_{\text{off}} C_b(\mathbf{X}, t), & \mathbf{X} \in \Gamma_0, & \end{aligned} \quad (22c)$$

$$\frac{\partial c_f(\mathbf{x}, t)}{\partial \mathbf{n}} = 0, \quad \mathbf{x} \in \Gamma_t^{f-} \setminus \Gamma_t, \quad (22d)$$

in which the domain Ω_t^{f-} is fixed. The advective step is treated with a semi-Lagrangian method using polyharmonic splines to reconstruct the function. The diffusion step is treated with a cut-cell finite volume method. The surface concentrations are solved for by extrapolating the fluid-phase field to the boundary and approximating the ODE.

3.3.1 Surface Reactions

Along the surface Γ_t , we allow for binding of the fluid-phase species to the boundary and for unbinding of the surface-bound species into the fluid, as described by equations (22b) and (22c). We extract a boundary mesh from the volumetric leaflet mesh described with C^0 elements. We

maintain a representation of both the surface concentration $C_b(\mathbf{X}, t)$ per unit reference area and the fluid concentration $c_f(\mathbf{X}, t)$ per unit current volume restricted to the boundary. These values are represented using Lagrangian basis functions $\{\psi_l(\mathbf{X})\}_{l=1}^{n_{bd}}$ in which n_{bd} is the number of nodes of the boundary mesh. We note these are the same basis functions used for the structural deformation, restricted to the surface. The concentrations along the boundary are accordingly

$$C_b(\mathbf{X}, t) = \sum_{l=1}^{n_{bd}} C_b^l(t) \psi_l(\mathbf{X}), \quad (23)$$

$$c_f(\mathbf{X}, t) = \sum_{l=1}^{n_{bd}} c_f^l(t) \psi_l(\mathbf{X}). \quad (24)$$

The values c_f^l are found by using a radial basis function interpolant as described in section 3.3.2 to extrapolate the values of $c_f(\mathbf{x}, t)$ to the surface. The nodal values C_b^l are found by solving the ODE in equation (22c) using a two stage Runge Kutta method. This finite element representation allows for easy evaluations of the flux from the boundary to the fluid.

To evaluate the boundary flux in equation (22b), we require the value of the Jacobian $J_s = \frac{d\mathbf{a}}{d\mathbf{A}}$ that converts areas in the reference configuration to areas in the current configuration. Because we are using a C^0 representation of the surface, the Jacobian is discontinuous at nodes. To obtain a continuous representation, we project J_s onto the finite element basis [21].

3.3.2 Reconstructions

Both the semi-Lagrangian step and the surface reactions involve reconstructing $c_f(\mathbf{x}, t)$ at various points in the domain. The details of the reconstruction procedure depend on where the reconstruction is being performed within the computational domain. Away from the boundary, we use the four closest grid points to $\mathbf{x}_{i,j}^n$ to form a bilinear interpolant. If there is not enough points to form the bilinear interpolant (e.g., near cut-cells), we use a radial basis function (RBF) interpolant [8, 37]. The RBF interpolant is constructed via a polyharmonic spline

$$q(\mathbf{x}) = \sum_{j=1}^k \lambda_j \|\mathbf{x} - \mathbf{x}_j\|^m + \sum_{j=1}^s \beta_j p_j(\mathbf{x}), \quad (25)$$

in which m is an odd integer and $p_j(\mathbf{x})$ form a set of s polynomial basis functions. The total number of points in the stencil k is chosen so that $k = 2m + 1$. We find the coefficients λ_j and β_j by requiring

$$q(\mathbf{x}_j) = f_j \text{ for } j = 1, \dots, k, \quad (26a)$$

$$\sum_{i=1}^s \lambda_i p_i(\mathbf{x}_j) = 0 \text{ for } j = 1, \dots, k. \quad (26b)$$

This results in a linear system for the coefficients, which is solved using a QR algorithm. In our computations, we set the integer $m = 3$ and use up to quadratic polynomials.

3.3.3 Cut Cell Geometries

To find cut cell volumes, we first calculate a signed distance function at each point $\mathbf{x}_{i+\frac{1}{2},j+\frac{1}{2}}$ to the structure. To do this, we first find intersections of the C^0 representation of the immersed structure with the background Eulerian grid. Additionally, for each element of the immersed structure, we calculate outward facing normals. We note that this requires a consistent traversal (e.g., counter-clockwise) of the structure to ensure a consistent facing normal. Then, for each point $\mathbf{x}_{i+\frac{1}{2},j+\frac{1}{2}}$ of the background grid, we find the projection of the point onto each element. If multiple minimal projections exist, we use the angle weighted average of the projections [1]. The sign of the distance is computed using the previously computed structure normal. Once we have the signed distances along each cut cell, we can compute partial cell volumes. Following Min and Gibou [27], we compute cell volumes by decomposing the cell into simplices, for which analytic formulas for the volume exist.

3.4 Time Stepping

In summary, the steps to advance the solution from time t^n to time t^{n+1} are:

1. Compute the cut cell geometries.
2. Perform a half step of the diffusion solve, evolving both the fluid-phase and the structure-bound concentration fields.
3. Solve the Navier-Stokes equations and update the position of the immersed structure.
4. Update the cut cell geometries using the new position of the immersed structure.
5. Perform a full step of the semi-Lagrangian method, using the velocities from the Navier-Stokes solve.
6. Perform a half step of the diffusion step, evolving the fluid-phase and surface-bound concentrations.

We determine an empirical scaling relationship between the time step size and the stiffness of the leaflet that maintains numerical stability under increasing leaflet stiffness. Specifically, we choose the time step such that

$$\Delta t = \frac{C_{\text{ts}}}{\sqrt{\max(C_{10})}}, \quad (27)$$

in which C_{ts} is chosen to be as large as possible.

4 Results

Table 1 provides the values of all relevant physical and numerical parameters. During the first two cycles, the binding and unbinding coefficient, k_{on} and k_{off} , are set to zero; afterward they are reset to their non-zero values. We emphasize that the binding and unbinding coefficients and the diffusion coefficient are artificially increased by several orders of magnitude compared to other clotting models [9, 24] to ensure that sufficient binding can occur within the duration of the simulation.

Table 1: Values of the parameters used in the simulation.

Structure parameters		Deposition and Fluid parameters	
κ	$20.17 \frac{\text{GPa}}{\text{cm}^2}$	k_{on}	$0.03321 \frac{\text{cm}^3}{\text{s platelet}}$
k_{stab}	58.4 MPa	k_{off}	$0.01 \frac{1}{\text{s}}$
C_{01}	3.25	D	$0.1 \frac{\text{cm}^2}{\text{s}}$
C_{10}^{min}	2.264 MPa	$C_{\text{b}}^{\text{max}}$	$1.41 \times 10^7 \frac{\text{platelet}}{\text{cm}^2}$
β	varies	$C_{\text{f}}^{\text{max}}$	$1.5 \times 10^5 \frac{\text{platelet}}{\text{cm}^3}$
		ρ	$1 \frac{\text{g}}{\text{cm}^3}$
		μ	$0.035 \frac{\text{g}}{\text{cm s}}$
Boundary model parameters			
R_{p}	$0.9046 \frac{\text{mmHg s}}{\text{mL}}$	$\tau_{1,\text{LA}}$	0.097 89 s
C	$1.950 \frac{\text{mL}}{\text{mmHg}}$	$\tau_{1,\text{LV}}$	0.0887 s
R_{c}	$0.042 \frac{\text{mmHg s}}{\text{mL}}$	$m_{1,\text{LA}}$	1.32
Q_{vein}	$6.2 \frac{\text{L}}{\text{min}}$	$m_{1,\text{LV}}$	2.404
Q_{LVOT}	$0.015 \frac{\text{mmHg s}}{\text{mL}}$	$\tau_{2,\text{LA}}$	0.1602 s
R_{MV}	$0.005 \frac{\text{mmHg s}}{\text{mL}}$	$\tau_{2,\text{LV}}$	0.4461 s
$E_{\text{max,LA}}$	$0.17 \frac{\text{mmHg}}{\text{mL}}$	$m_{2,\text{LA}}$	13.1
$E_{\text{min,LA}}$	$0.08 \frac{\text{mmHg}}{\text{mL}}$	$m_{2,\text{LV}}$	20.952
$E_{\text{min,LV}}$	$0.0265 \frac{\text{mmHg}}{\text{mL}}$	$E_{\text{max,LV}}$	$0.16 \frac{\text{mmHg}}{\text{mL}}$

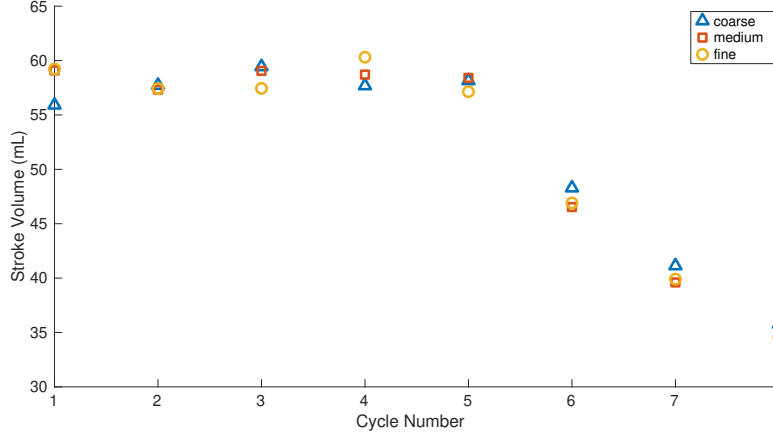


Figure 2: The stroke volume for a coarse, medium, and fine grid is computed by the methods described in section 4.3. All simulations are performed with $\beta = 100$ and with binding occurring on both leaflets. We observe clear convergence as the mesh is refined.

4.1 Convergence Study

We first demonstrate convergence on the full problem. We run simulations using three different meshes, characterized by the number of elements spanning the leaflet in the thin direction. We generate three different resolutions of meshes with maximum element edge lengths of 0.32, 0.24, and 0.18 mm, which correspond to 2, 3, and 4 elements across the width of the leaflets, respectively. The background Cartesian grid is refined such that there is approximately one structural mesh node per grid cell. To assess convergence, we considered the stroke volume and the total surface accumulation on the leaflet. Figure 2 shows the stroke volume for 8 cycles. The computation of the stroke volume will be described in section 4.3. We observe similar stroke volumes at all cycle numbers, and a clear tendency towards convergence for the first two cycles and last three cycles. Figure 3 shows the total surface accumulation

$$\int_{\Gamma_t} \frac{C_b(\mathbf{X}, t)}{C_b^{\max}} J_s d\mathbf{A}, \quad (28)$$

over time for the last two cycles. We again observe a clear indication of convergence. In what remains, we use the coarse mesh, consisting of two elements across the leaflet.

4.2 Leaflet Deposition

Figure 4 shows snapshots from a simulation with deposition on the right leaflet. The right leaflet is substantially stiffer than the left, and the predominant flow through the valve is shifted towards the left leaflet. Figure 5 shows snapshots with deposition on both leaflets. Here, both leaflets become stiff and open less over time.

To assess the opening of the valve, we project the leaflets onto the valve ring, as shown in figure 6a. The opening area is then normalized by the fully open valve. Figure 6b shows the

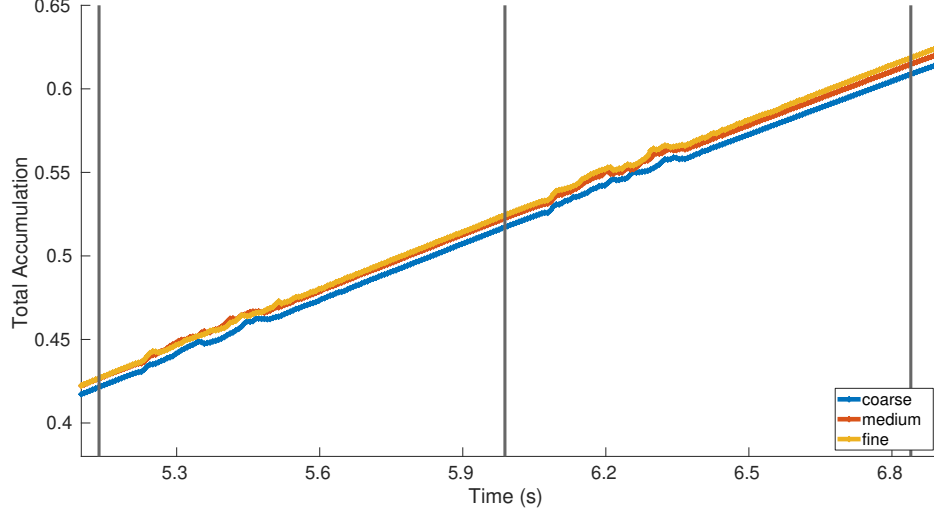


Figure 3: The total surface accumulation $\int_{\Gamma_t} \frac{C_b(\mathbf{X}, t)}{C_b^{\max}} J_s d\mathbf{X}$ along the leaflet for a coarse, medium, and fine grid. All simulations are run with $\beta = 100$ and with binding occurring on both leaflets. We observe clear convergence as the mesh is refined.

normalized open valve area over each cycle for deposition on both leaflets, as we increase the maximum stiffness β . For lower maximal stiffnesses, we observe similar normalized open valve areas compared to a simulation with no deposition. For larger maximum stiffness, we observe a smaller normalized open valve area as more deposition occurs. Figure 6c compares the normalized open valve area for deposition on both leaflets versus on only the right leaflet for the same maximum stiffness. When deposition occurs on only the right leaflet, the normalized open valve area still decreases compared to no accumulation, but does not realize as dramatic decreases. The left leaflet, which has a constant stiffness over time, compensates and opens more as the right leaflet stiffens.

We additionally compare the total accumulation of the surface concentration on the leaflet. Figure 7 shows the maximum and minimum accumulations C_b/C_b^{\max} across the leaflet. Because the diffusion coefficient is large compared to the reaction rates, there is always sufficient fluid-phase platelets to bind to the leaflets, and accordingly, a consistent rate of binding to the surface. By the end of the simulation, only approximately 23% of the carrying capacity of the surface bound platelets is bound. The minimum concentration sees periodic jumps while the maximum concentration is monotonically increasing. The periodic jumps are due to the physical location of the minimum and maximum. The minimum is located near the position where the leaflet attaches to the aortic wall. This location sees the largest changes in area as the valve opens. The maximum concentration is found on the tips of the leaflet, which move through regions of high fluid-phase concentration. The tip of the leaflets deform less upon opening and closing of the valve, leading to a steady surface bound concentration field. Figure 8 shows the velocity magnitude during the final cycle near peak systole. We observe a vortex in the sinus region that grows in strength as we

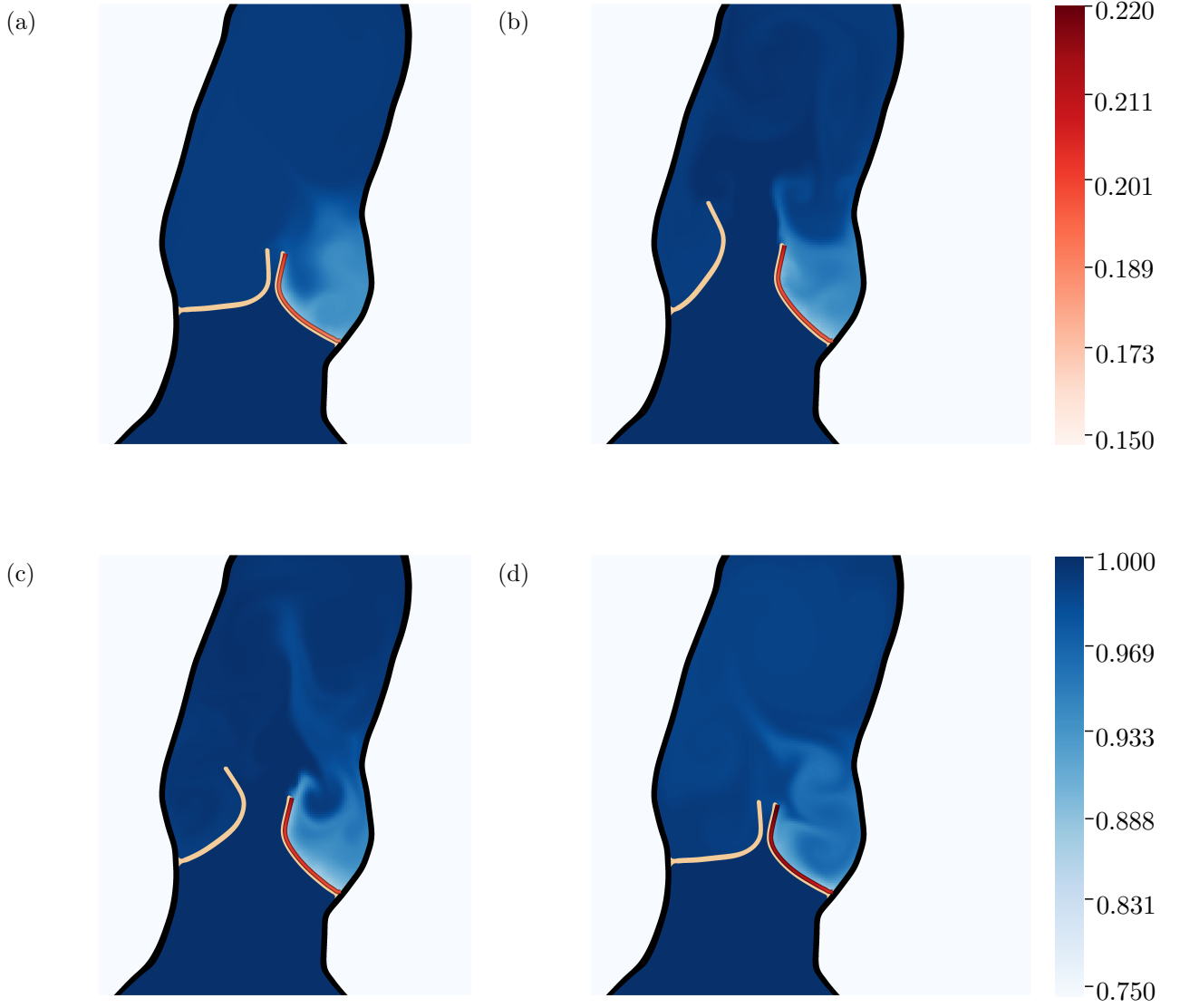


Figure 4: Snapshots from a simulation in which deposition happens on the right leaflet during peak diastole (a), peak systole (b), end systole (c), and peak diastole (d) over the last cycle showing the fluid-phase concentration fraction c_f/c_f^{\max} and the surface accumulation C_b/C_b^{\max} . This simulation uses $\beta = 600$. Notice that the right leaflet is considerably stiffer than the left leaflet, and the fluid concentration depletes in the aortic root.

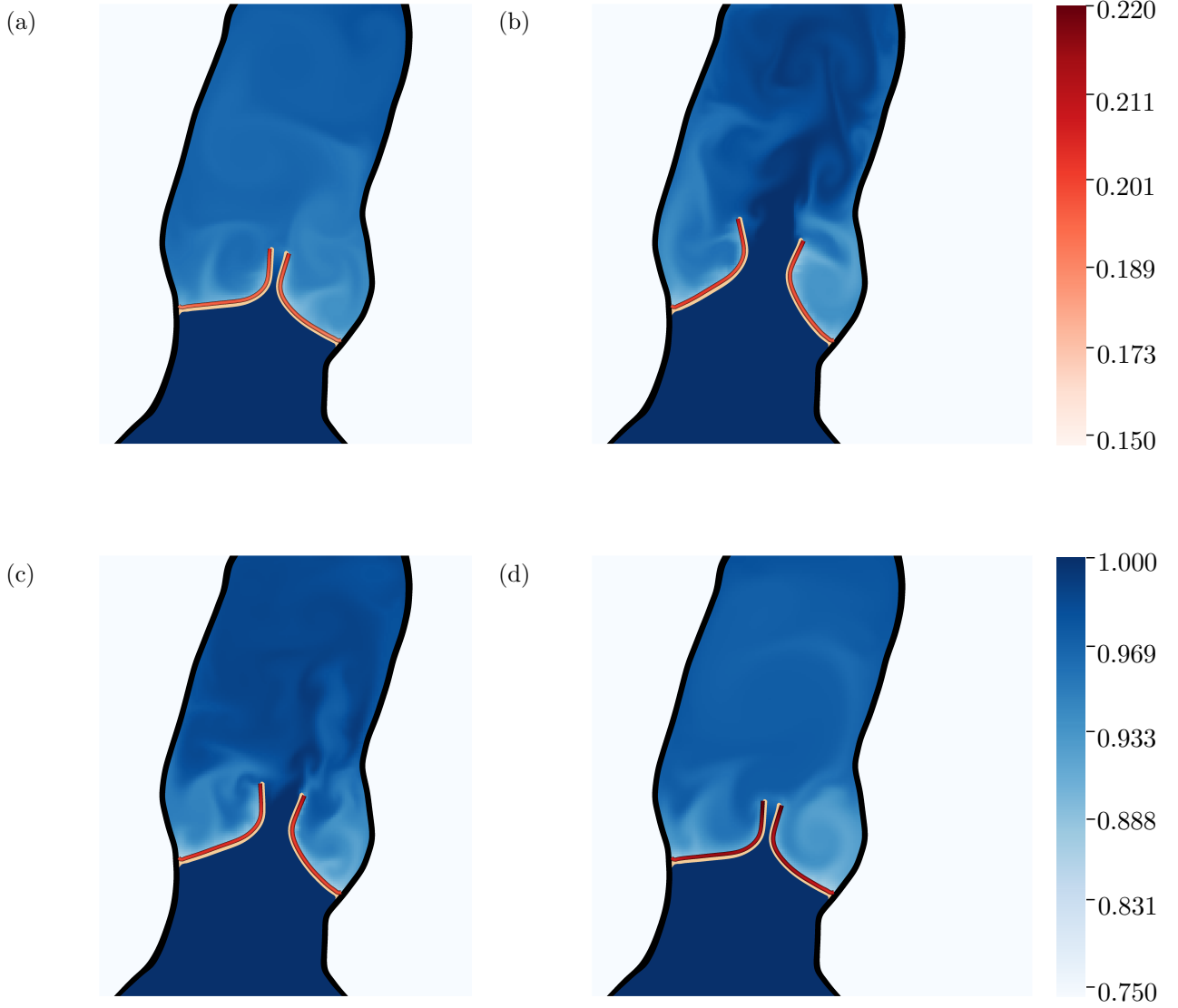


Figure 5: Snapshots from a simulation in which deposition happens on both leaflets during peak diastole (a), peak systole (b), end systole (c), and peak diastole (d) over the last cycle showing the fluid-phase concentration fraction c_f/c_f^{\max} and the surface accumulation C_b/C_b^{\max} . This simulation uses $\beta = 600$. Both leaflets are considerably stiffer than those in figure 4.

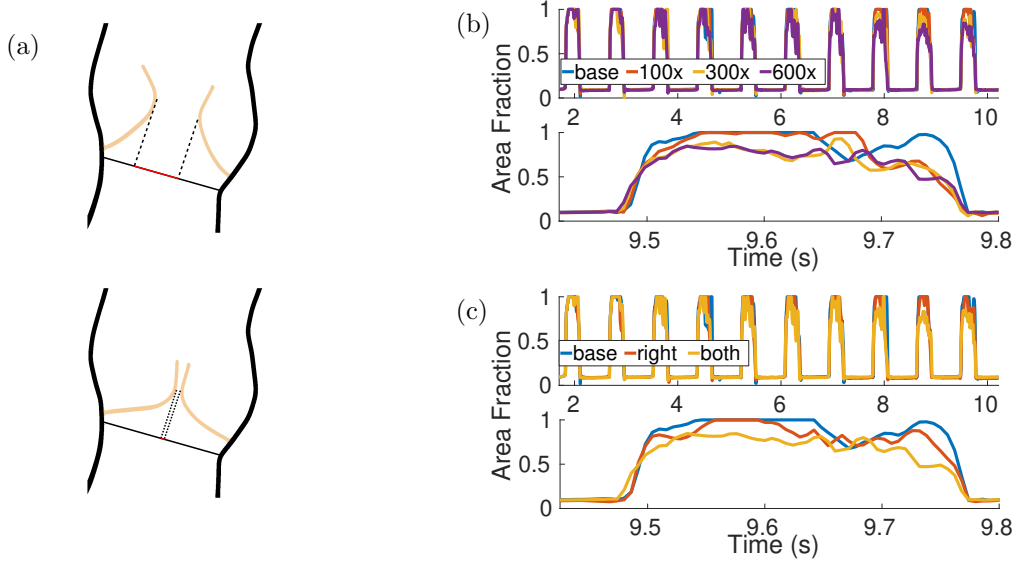


Figure 6: The computed normalized open valve area over time. Panel (a) depicts the computation of the normalized open valve area. The open area of the valve is projected onto the valve ring, and then normalized by the area of the fully opened valve. Panel (b) depicts the normalized open valve area over time for accumulation on both leaflets as β increases during the entire simulation and during only the last cycle. Notice that as the leaflets get stiffer, the normalized open valve area decreases. Panel (c) depicts the normalized open valve area over time for accumulation on the right leaflet or both leaflets during all the cycles and during only the last cycle. Notice that if accumulation occurs on both leaflets, the normalized open valve area decreases more than if accumulation occurs on a single leaflet.

increase the maximum stiffness. This vortex is not present when accumulation occurs exclusively on a single leaflet, but is present when there is no accumulation.

4.3 Pressure and Stroke Volume

We now quantify valve's resistance to the flow at different binding rates. We measure the pressures at locations just upstream and downstream of the valve, as shown in figures 9 and 10. We observe a marginal increase in the pressures upstream of the valve; however, there are sharp decreases in the aortic pressures as we increase stiffness. A similar trend is observed with deposition on only the right leaflet, although the differences are not as pronounced.

The stroke volume is computed by integrating the flow rate through the edge of the computational domain that is inside the aorta. To convert the two dimensional flow rates into a volumetric flow rate, we assume the two dimensional flow rate is constant along a rectangle that has similar area as that of the cross-section of a physical aorta. We note that this is the same flow rate used to couple the boundary condition model with the FSI computation. We observe notable oscillations in the flow rates when the valve closes (not shown). Therefore, we compute flow rates only when

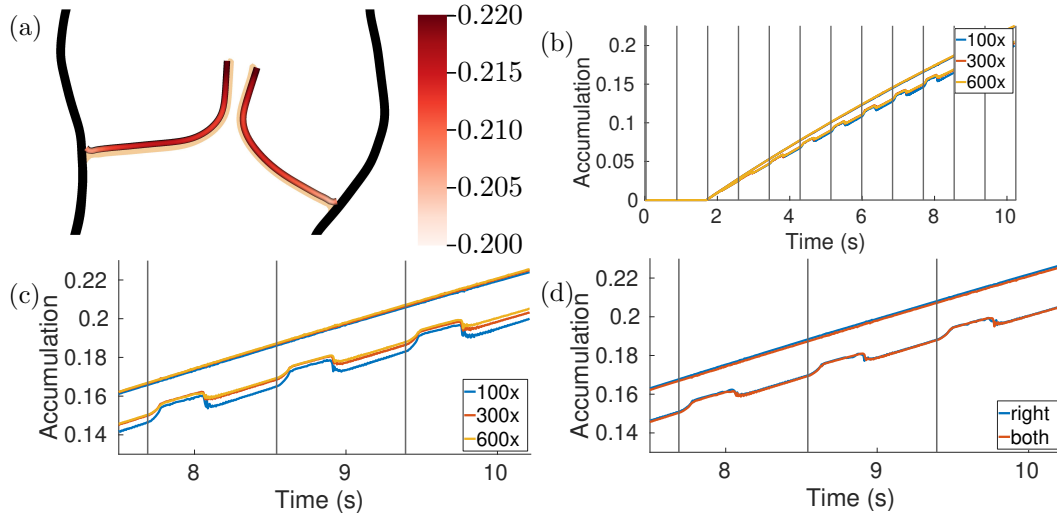


Figure 7: (a) The accumulation C_b/C_b^{\max} along the leaflets at the end of the simulation with $\beta = 600$. (b) The minimum and maximum accumulation C_b/C_b^{\max} on the leaflets. Panel (c) highlights the accumulation over the last three cycles for accumulation on both leaflets for three values of β . In panel (d), the accumulation is shown for accumulation only on the right leaflet versus both leaflets with $\beta = 600$. The vertical lines denote the beginning of systole. There is a consistent accumulation of material on the leaflets. The minimum concentration occurs where the leaflet attaches to the aortic wall.

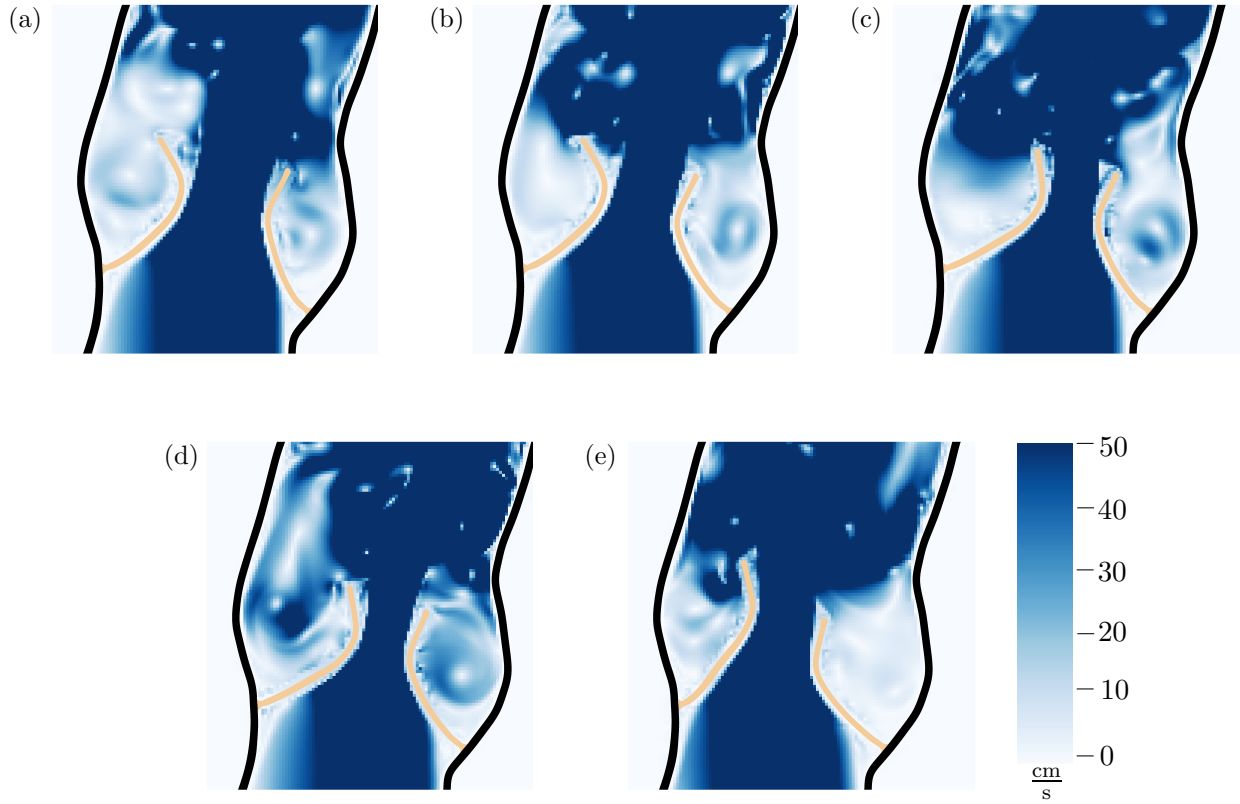


Figure 8: The magnitude of the velocity field at peak systole during the last cycle for (a) no accumulation, (b) $\beta = 100$ with accumulation on both leaflets, (c) $\beta = 300$ with accumulation on both leaflets, (d) $\beta = 600$ with accumulation on both leaflets, and (e) $\beta = 600$ with accumulation on only the right leaflet. Notice the presence of a vortex in the right sinus that is absent if accumulation only occurs on one leaflet.

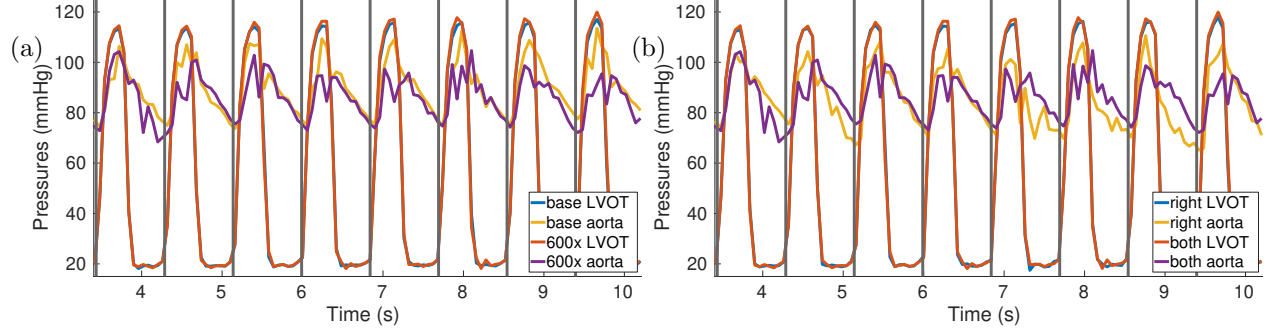


Figure 9: The pressures just upstream and downstream of the valve. Panel (a) compares the pressures for no accumulation and accumulation on both leaflets with $\beta = 600$. Panel (b) compares pressures for accumulation on only the right leaflet and both leaflets, both having $\beta = 600$. While the upstream pressure increases mildly, the downstream pressures decrease by between 5 and 10 mmHg.

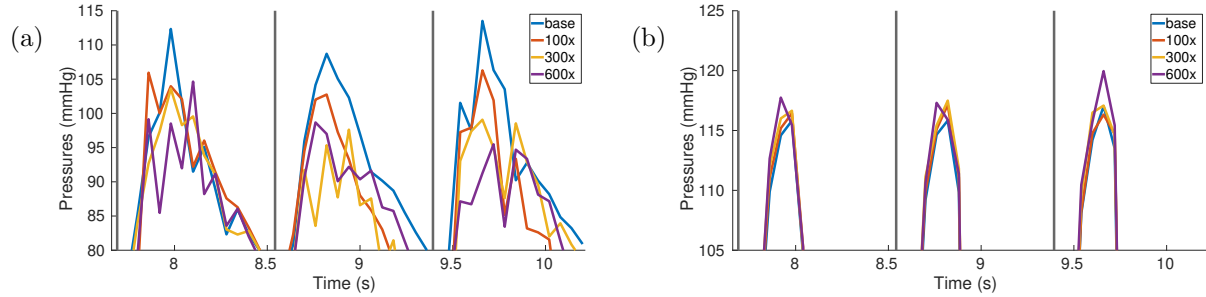


Figure 10: The pressures for accumulation during the last three cycles for accumulation on both leaflets with $\beta = 0, 100, 300$, and 600 . The aortic side pressures are shown in panel (a). The left ventricle side pressures are shown in panel (b). While the upstream pressure increases mildly, the downstream pressures decrease by between 5 and 10 mmHg.

the valve is open. The stroke volume is shown in figure 11. When compared to normal case, in which there is no deposition, there is a consistent decrease in stroke volume as more fluid-phase platelets deposit over the leaflets. The reduction in stroke volume is not monotonically decreasing. We found no significant difference in stroke volume when deposition occurs on only one leaflet as compared to both leaflets.

5 Conclusions

This study presents numerical methods incorporating both deposition and fluid-structure interaction to simulate leaflet thrombosis. The simplified thrombosis model serves as a stepping stone to demonstrate the capabilities of our simulation approach that includes concentration fields de-

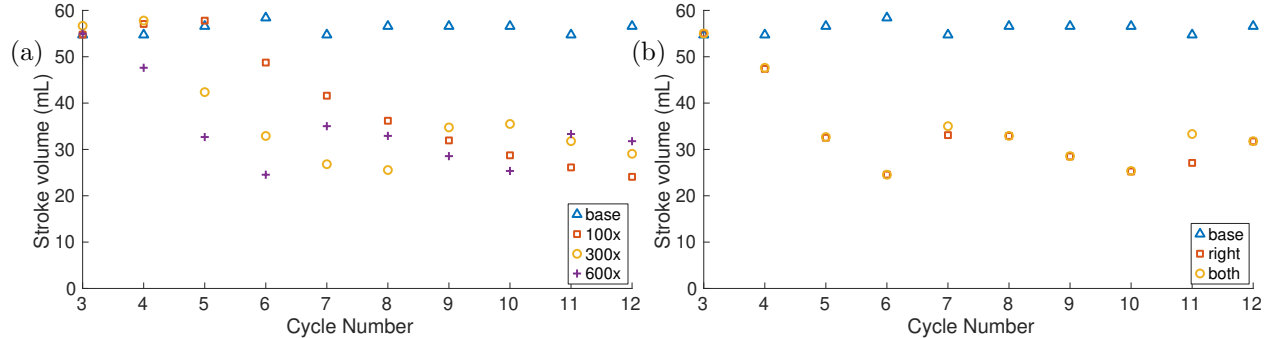


Figure 11: The stroke volume for each cycle. The stroke volume for accumulation on both leaflets as β increases are shown in panel (a). The stroke volume for accumulation on both leaflets versus only the right leaflet with $\beta = 600$ are shown in panel (b). While in all cases, the stroke volume decreases when compared to $\beta = 0$, the decrease is not monotonic as we increase β . We observe minimal differences in stroke volume when accumulation occurs on one leaflet compared to both.

scribing fluid-phase platelets and structure-bound platelets. Platelets can deposit over the leaflet surface, and bound platelets can dissociate back into the fluid. In our model, the stiffness of the leaflet is a function of the bound platelet concentration. We have shown that our model is capable of realizing decreased stroke volume, without fully occluding the aortic valve. The results also show that the stiffness of the valve can lead to a variety of flow features in the sinus of Valsalva region. These flow features affect the amount of material that is locally present to deposit over the leaflets. Further, we have demonstrated the convergence of the discretization via both stroke volume and the total surface accumulation.

Extensions of this model to three dimensions require an efficient method for solving the advection-diffusion equation in complex, time-evolving domains. The method utilized here requires the computation of cut-cell volumes and intersections, which remain challenging in three spatial dimensions. Recent approaches to this class of problems include mesh-free RBF-FD methods [37] and volume penalization methods [39]. The implementation of a more physiological model of thrombosis remains an important future work. A primary roadblock is the disparate time scales present in thrombosis. While the heart beats on the order of seconds, blood clots can form in hours to days. The use of conditionally stable time stepping limits this current model to timesteps that resolve the fastest timescale, which in this model is that of the fluid-structure interaction. Recent work in multiscale time stepping algorithms [11, 12] could enable extensions of our modeling framework to enable such long-time simulations. While platelet deposition is important and the beginning step of thrombus formation, a significant portion of the clot is from coagulation and fibrin mesh formation. However, a complete model of thrombosis will require a model of the growth of the blood clot into the fluid [9, 24]. The development of such a model that incorporates FSI is ongoing.

The new approaches described herein should be considered an important steppingstone for thrombosis models in many different contexts. This model is the first of its kind to incorporate

both adhesion of a surface concentration to the surface of the leaflets and feedback into the fluid-structure interaction. Further, this model can be adapted to model deposition or absorption along other moving boundaries, such as particulate flow in the lungs or drug absorption in the gut.

Acknowledgements

We acknowledge funding from the NIH (Awards U01HL143336 and R01HL157631) and NSF (OAC 1652541 and OAC 1931516).

References

- [1] J. A. Bærentzen and H. Aanæs. “Signed distance computation using the angle weighted pseudonormal”. *IEEE Transactions on Visualization and Computer Graphics* 11.3 (2005), pp. 243–253.
- [2] S. Balay, S. Abhyankar, M. F. Adams, J. Brown, P. Brune, K. Buschelman, L. Dalcin, V. Eijkhout, W. D. Gropp, D. Karpeyev, D. Kaushik, M. G. Knepley, L. Curfman McInnes, K. Rupp, B. F. Smith, S. Zampini, and H. Zhang. *PETSc Users Manual*. Tech. rep. ANL-95/11 - Revision 3.13. Argonne National Laboratory, 2015.
- [3] S. Balay, S. Abhyankar, M. Adams, J. Brown, P. Brune, K. Buschelman, L. Dalcin, A. Dener, V. Eijkhout, W. Gropp, D. Karpeyev, D. Kaushik, M. Knepley, D. May, L. C. McInnes, R. T. Mills, T. Munson, K. Rupp, P. Sanan, B. Smith, S. Zampini, H. Zhang, and H. Zhang. *PETSc Web page*. <https://www.mcs.anl.gov/petsc>. 2019.
- [4] S. Balay, W. D. Gropp, L. C. McInnes, and B. F. Smith. “Efficient Management of Parallelism in Object-Oriented Numerical Software Libraries”. *Modern Software Tools for Scientific Computing*. Ed. by E. Arge, A. M. Bruaset, and H. P. Langtangen. Birkhäuser Press, 1997, pp. 163–202.
- [5] A. Barrett, A. L. Fogelson, and B. E. Griffith. “A hybrid semi-Lagrangian cut cell method for advection-diffusion problems with Robin boundary conditions in moving domains”. *Journal of Computational Physics* 449 (2022), p. 110805.
- [6] S. L. Diamond, J. Purvis, M. Chatterjee, and M. H. Flamm. “Systems biology of platelet-vessel wall interactions”. *Frontiers in Physiology* 4 (2013).
- [7] J. Du and A. L. Fogelson. “A Two-phase mixture model of platelet aggregation”. *Mathematical Medicine and Biology* 35.2 (2018), pp. 225–256.
- [8] N. Flyer, B. Fornberg, V. Bayona, and G. A. Barnett. “On the role of polynomials in RBF-FD approximations: I. Interpolation and accuracy”. *Journal of Computational Physics* 321 (2016), pp. 21–38.

- [9] A. L. Fogelson and R. D. Guy. “Immersed-boundary-type models of intravascular platelet aggregation”. *Computer Methods in Applied Mechanics and Engineering* 197.25-28 (2008), pp. 2087–2104.
- [10] A. L. Fogelson, Y. H. Hussain, and K. Leiderman. “Blood Clot Formation under Flow: The Importance of Factor XI Depends Strongly on Platelet Count”. *Biophysical Journal* 102.1 (2012), pp. 10–18.
- [11] S. Frei and T. Richter. “Efficient Approximation of Flow Problems With Multiple Scales in Time”. *Multiscale Modeling & Simulation* 18.2 (2020), pp. 942–969.
- [12] S. Frei, T. Richter, and T. Wick. “Long-term simulation of large deformation, mechano-chemical fluid-structure interactions in ALE and fully Eulerian coordinates”. *Journal of Computational Physics* 321 (2016), pp. 874–891.
- [13] T. C. Gasser, R. W. Ogden, and G. A. Holzapfel. “Hyperelastic modelling of arterial layers with distributed collagen fibre orientations”. *Journal of The Royal Society Interface* 3.6 (2006), pp. 15–35.
- [14] B. E. Griffith. *IBAMR: an adaptive and distributed-memory parallel implementation of the immersed boundary method*. 2014.
- [15] B. E. Griffith. “An accurate and efficient method for the incompressible Navier-Stokes equations using the projection method as a preconditioner”. *Journal of Computational Physics* 228.20 (2009), pp. 7565–7595.
- [16] B. E. Griffith and X. Luo. “Hybrid finite difference/finite element immersed boundary method”. *International Journal for Numerical Methods in Biomedical Engineering* 33.12 (2017), e2888.
- [17] H. Hatoum, S. Singh-Gryzbon, F. Esmailie, P. Ruile, F.-J. Neumann, P. Blanke, V. H. Thourani, A. P. Yoganathan, and L. P. Dasi. “Predictive Model for Thrombus Formation After Transcatheter Valve Replacement”. *Cardiovascular Engineering and Technology* 12.6 (2021), pp. 576–588.
- [18] R. D. Hornung and S. R. Kohn. “Managing application complexity in the SAMRAI object-oriented framework”. *Concurrency and Computation: Practice and Experience* 14.5 (2002), pp. 347–368.
- [19] B. S. Kirk, J. W. Peterson, R. H. Stogner, and G. F. Carey. “libMesh : a C++ library for parallel adaptive mesh refinement/coarsening simulations”. *Engineering with Computers* 22.3-4 (2006), pp. 237–254.
- [20] A. R. Kivi, N. Sedaghatizadeh, B. S. Cazzolato, A. C. Zander, R. Roberts-Thomson, A. J. Nelson, and M. Arjomandi. “Fluid structure interaction modelling of aortic valve stenosis: Effects of valve calcification on coronary artery flow and aortic root hemodynamics”. *Computer Methods and Programs in Biomedicine* 196 (2020), p. 105647.
- [21] E. M. Kolahdouz, A. P. S. Bhalla, B. A. Craven, and B. E. Griffith. “An immersed interface method for discrete surfaces”. *Journal of Computational Physics* 400 (2020), pp. 1–41.

- [22] J. H. Lee, L. N. Scotten, R. Hunt, T. G. Caranasos, J. P. Vavalle, and B. E. Griffith. “Bio-prosthetic aortic valve diameter and thickness are directly related to leaflet fluttering: Results from a combined experimental and computational modeling study”. *JTCVS Open* 6 (2021), pp. 60–81.
- [23] J. H. Lee and B. E. Griffith. “On the Lagrangian-Eulerian coupling in the immersed finite element/difference method”. *Journal of Computational Physics* 457 (2022), p. 111042.
- [24] K. Leiderman and A. L. Fogelson. “Grow with the flow: A spatial-temporal model of platelet deposition and blood coagulation under flow”. *Mathematical Medicine and Biology* 28.1 (2011), pp. 47–84.
- [25] R. R. Makkar and T. Chakravarty. “Transcatheter Aortic Valve Thrombosis”. *JACC: Cardiovascular Interventions* 10.7 (2017), pp. 698–700.
- [26] R. R. Makkar, G. Fontana, H. Jilaihawi, T. Chakravarty, K. F. Kofoed, O. De Backer, F. M. Asch, C. E. Ruiz, N. T. Olsen, A. Trento, J. Friedman, D. Berman, W. Cheng, M. Kashif, V. Jehnin, C. A. Kliger, H. Guo, A. D. Pichard, N. J. Weissman, S. Kapadia, E. Manasse, D. L. Bhatt, M. B. Leon, and L. Søndergaard. “Possible Subclinical Leaflet Thrombosis in Bioprosthetic Aortic Valves”. *New England Journal of Medicine* 373.21 (2015), pp. 2015–2024.
- [27] C. Min and F. Gibou. “Geometric integration over irregular domains with application to level-set methods”. *Journal of Computational Physics* 226.2 (2007), pp. 1432–1443.
- [28] K. Murdock, C. Martin, and W. Sun. “Characterization of mechanical properties of pericardium tissue using planar biaxial tension and flexural deformation”. *Journal of the Mechanical Behavior of Biomedical Materials* 77 (2018), pp. 148–156.
- [29] J. P. Murgio, N. Westerhof, J. P. Giolma, and S. A. Altobelli. “Aortic input impedance in normal man: relationship to pressure wave forms.” *Circulation* 62.1 (1980), pp. 105–116.
- [30] J. P. Mynard, M. R. Davidson, D. J. Penny, and J. J. Smolich. “A simple, versatile valve model for use in lumped parameter and one-dimensional cardiovascular models”. *International Journal for Numerical Methods in Biomedical Engineering* 28.6-7 (2012), pp. 626–641.
- [31] R. Plitman Mayo, H. Yaakovovich, A. Finkelstein, S. C. Shadden, and G. Marom. “Numerical models for assessing the risk of leaflet thrombosis post-transcatheter aortic valve-in-valve implantation”. *Royal Society Open Science* 7.12 (2020), p. 201838.
- [32] R. Ramana, C. Morreale, S. Kothari, L. M. Moura, P. Best, M. Burke, and N. M. Rajamannan. “Calcification and Thrombosis as Mediators of Bioprosthetic Valve Deterioration”. *Structural Heart* 3.2 (2019), pp. 106–109.
- [33] W. J. Rider, J. A. Greenough, and J. R. Kamm. “Accurate monotonicity- and extrema-preserving methods through adaptive nonlinear hybridizations”. *Journal of Computational Physics* 225.2 (2007), pp. 1827–1848.

- [34] L. Rosseel, O. De Backer, and L. Søndergaard. “Clinical Valve Thrombosis and Subclinical Leaflet Thrombosis Following Transcatheter Aortic Valve Replacement: Is There a Need for a Patient-Tailored Antithrombotic Therapy?” *Frontiers in Cardiovascular Medicine* 6 (2019).
- [35] Y. Sahasakul, W. D. Edwards, J. M. Naessens, and A. Tajik. “Age-related changes in aortic and mitral valve thickness: Implications for two-dimensional echocardiography based on an autopsy study of 200 normal human hearts”. *The American Journal of Cardiology* 62.7 (1988), pp. 424–430.
- [36] G. Schymik, H. Schröfel, M. Heimeshoff, A. Luik, M. Thoenes, A. Luik, M. Thoenes, and L. Mandinov. “How to Adapt the Implantation Technique for the New SAPIEN 3 Transcatheter Heart Valve Design”. *Journal of Interventional Cardiology* 28.1 (2015), pp. 82–89.
- [37] V. Shankar and A. L. Fogelson. “Hyperviscosity-based stabilization for radial basis function-finite difference (RBF-FD) discretizations of advection–diffusion equations”. *Journal of Computational Physics* 372 (2018), pp. 616–639.
- [38] N. Stergiopoulos, B. E. Westerhof, and N. Westerhof. “Total arterial inertance as the fourth element of the windkessel model”. *American Journal of Physiology-Heart and Circulatory Physiology* 276.1 (1999), H81–H88.
- [39] R. Thirumalaisamy, N. A. Patankar, and A. P. S. Bhalla. “Handling Neumann and Robin boundary conditions in a fictitious domain volume penalization framework”. *Journal of Computational Physics* 448 (2022), p. 110726.
- [40] A. Tosenberger, F. Ataullakhanov, N. Bessonov, M. Panteleev, A. Tokarev, and V. Volpert. “Modelling of platelet–fibrin clot formation in flow with a DPD–PDE method”. *Journal of Mathematical Biology* 72.3 (2016), pp. 649–681.
- [41] B. Vadala-Roth, S. Acharya, N. A. Patankar, S. Rossi, and B. E. Griffith. “Stabilization approaches for the hyperelastic immersed boundary method for problems of large-deformation incompressible elasticity”. *Computer Methods in Applied Mechanics and Engineering* 365 (2020), p. 112978.
- [42] K. Vahidkhah, S. Javani, M. Abbasi, P. N. Azadani, A. Tandar, D. Dvir, and A. N. Azadani. “Blood Stasis on Transcatheter Valve Leaflets and Implications for Valve-in-Valve Leaflet Thrombosis”. *The Annals of Thoracic Surgery* 104.3 (2017), pp. 751–759.
- [43] Z. Wu, Z. Xu, O. Kim, and M. Alber. “Three-dimensional multi-scale model of deformable platelets adhesion to vessel wall in blood flow”. *Philosophical Transactions of the Royal Society A: Mathematical, Physical and Engineering Sciences* 372.2021 (2014), p. 20130380.
- [44] P. A. Yushkevich, J. Piven, H. Cody Hazlett, R. Gimpel Smith, S. Ho, J. C. Gee, and G. Gerig. “User-Guided 3D Active Contour Segmentation of Anatomical Structures: Significantly Improved Efficiency and Reliability”. *Neuroimage* 31.3 (2006), pp. 1116–1128.

- [45] P. A. Yushkevich, J. Piven, H. C. Hazlett, R. G. Smith, S. Ho, J. C. Gee, and G. Gerig. “User-guided 3D active contour segmentation of anatomical structures: Significantly improved efficiency and reliability”. *NeuroImage* 31.3 (2006), pp. 1116–1128.
- [46] P. Zhang, C. Gao, N. Zhang, M. J. Slepian, Y. Deng, and D. Bluestein. “Multiscale Particle-Based Modeling of Flowing Platelets in Blood Plasma Using Dissipative Particle Dynamics and Coarse Grained Molecular Dynamics”. *Cellular and Molecular Bioengineering* 7.4 (2014), pp. 552–574.